

Rechargeable Photoactive Zn-Air Batteries Using NiCo_2S_4 as an Efficient Bifunctional Photocatalyst towards OER/ORR at the Cathode

Sangchai Sarawutanukul,^[a, b] Chanikarn Tomon,^[a, b] Salatan Duangdangchote,^[a, b] Nutthaphon Phattharasupakun,^[a, b] and Montree Sawangphruk^{*[a, b]}

Using free solar energy in oxygen evolution reaction (OER) and oxygen reduction reaction (ORR) electrocatalysts to enhance the efficiency of zinc-air batteries (ZABs) has not yet been widely investigated. Herein, we report a photoactive bifunctional catalyst of spinel-type NiCo_2S_4 (NCS) urchin-like structure with rich mesopores and direct band gap energies of ca. 1.4 and 2.4 eV. The NCS catalyst exhibits high catalytic activities for both OER ($\eta=338$ mV at 10 mA cm^{-2}) and ORR ($\eta=475$ mV at $E_{1/2}$), comparable to that of the state-of-the-art counterparts (e.g., Pt/C for ORR, RuO_2 for OER). Under light illumination, the p-type photoactive NCS catalyst can absorb visible light, generating photogenerated holes and photoelectrons via the

photoelectric effect for direct conversion of photoenergy into electric energy with increasing kinetics charge transfer process and provides ca. 10 and 18.5% lower OER and ORR overpotentials, respectively than those under the dark condition. In addition, the as-fabricated zinc-air battery with the photoactive NCS as the cathode exhibits decrease in voltage gap from 0.82 to 0.60 V with an increasing round-trip efficiency from 59.2% to 68.8% after exposed to visible light. The zinc-air battery with a reversible redox reaction for the simultaneous conversion of chemical and photoenergy into electric energy could open a new pathway for the utilization of a single energy conversion and storage device.

1. Introduction

Due to the rapid increase of energy crisis and global warming issues, the development of high-performance energy storage and energy conversion systems has become one of the most urgent challenges to reduce the consumption of conventional fossil fuel.^[1] Among the energy storage and conversion systems, the integration of solar energy conversion using semiconducting photocatalysts such as ZnS , CdS , TiO_2 , Fe-N-C and NiCo_2O_4 ^[2] and electrochemical energy storage systems such as supercapacitors,^[3] Li-ion batteries, and metal-air batteries has recently attracted considerable attention as an efficient and promising technology to address the aforementioned problem.^[4]

Zn-air battery (ZAB) has been considered as an attractive candidate in electrochemical energy storages because of its prominent advantages such as a high energy density (1086 Wh kg⁻¹), a flat working potential (1.67 V), good safety, low cost, and environmentally friendly.^[5] Despite their enormous prom-

ises for commercialization, there are several major challenges associated with ZABs including a sluggish oxygen reduction reaction (ORR), a low oxygen evolution reaction (OER) kinetics, and a large overpotential.^[6] To date, Pt/C is recognized as a highly efficient ORR catalyst and RuO_2 is promising in OER.^[7] However, the extensive utilization of these precious metals is limited by their high cost, scarcity, and poor durability.^[8] Therefore, the incorporation of light illumination into a photoactive bifunctional catalyst is very challenging to accelerate the sluggish OER and ORR or reducing the polarization of Zn-air batteries for achieving high energy density.^[9]

Recently, a semiconductor NiCo_2O_4 (NCO) with a spinel structure has been widely investigated as a bifunctional OER/ORR catalyst due to the cooperative contribution from both nickel and cobalt ions with mixed-valence states ($\text{Ni}^{2+}/\text{Ni}^{3+}$, $\text{Co}^{2+}/\text{Co}^{3+}$) in the crystal structure.^[10] When the oxygen atoms in the spinel structure are substituted with sulfur atoms, the electrical conductivity of spinel sulfides increases ca. 100 folds,^[11] which is significant for excellent electrochemical performance.^[12] Furthermore, due to the lower electronegativity and larger atomic radius of sulfur as compared to oxygen, the NiCo_2S_4 (NCS) exhibits a more flexible structure, richer redox properties, and suitable band structure over NiCo_2O_4 .^[13] Based on all these properties, a spinel metal sulfide could be ideal as a photoactive bifunctional OER and ORR catalyst. However, to the best of our knowledge, there is no previous report on the concept of enhancing ZABs with light using p-type semiconductor NCS as a photo-responsive bifunctional catalyst for the OER and ORR. Herein, we report the successful preparation of mesoporous NCO and NCS microspheres by a self-template method together with the following sulfidation treatment

[a] S. Sarawutanukul, C. Tomon, S. Duangdangchote, N. Phattharasupakun, Prof. Dr. M. Sawangphruk
Department of Chemical and Biomolecular Engineering,
School of Energy Science and Engineering,
Vidyasirimedhi Institute of Science and Technology,
555 Moo 1 Payupnai, Wangchan District, Rayong 21210 (Thailand)
E-mail: montree.s@vistec.ac.th

[b] S. Sarawutanukul, C. Tomon, S. Duangdangchote, N. Phattharasupakun, Prof. Dr. M. Sawangphruk
Center of Excellence for Energy Storage Technology (CEST),
Vidyasirimedhi Institute of Science and Technology,
555 Moo 1 Payupnai, Wangchan District, Rayong 21210 (Thailand)

 Supporting information for this article is available on the WWW under <https://doi.org/10.1002/batt.201900205>

process via an ion-exchange reaction. The NCO and NCS were then employed as photoelectrodes in ZABs. The unique morphology of NCS with richer active sites exhibits a lower overpotential of OER ($\eta = 338$ mV at 10 mA cm^{-2}) and ORR ($\eta = 475$ mV at $E_{1/2}$) as compared with that of NCO and other precious metal catalysts. In addition, the energy level of NCS shows lower direct band gaps of 1.4 eV and 2.4 eV than those of NCO. Interestingly, it is worth pointing out that the p-type semiconductor NCS can absorb visible light generating photo-generated holes and photoelectrons via the photoelectric effect. Furthermore, the photo-assisted rechargeable Zn-air batteries using the photoactive NCS as the air electrode exhibit a low charge-discharge voltage gap (~ 0.82 V at 2 mA cm^{-2}) and a remarkable cycling stability over 60 cycles without catalyst decaying as compared with the-state-of-the-art Pt/C and RuO₂. Upon the light illumination, the charge-discharge profiles of NCS-based ZAB show an extremely low charge voltage of 1.91 V and a high discharge voltage of 1.32 V with a high round-trip efficiency of $\sim 68.8\%$. This photoactive OER and ORR NCS at the cathode enables to significantly enhance the charge storage performance of Zn-air battery. Thus, this work may lead to new development for advanced photoactive energy storage systems.

Experimental Section

Synthesis of urchin-like Ni–Co precursor nanospheres

The chemicals in the synthesis process are all analytical grade and used without further treatment. Firstly, 4 mmol of Ni(NO₃)₂·6H₂O and 8 mmol of Co(NO₃)₂·6H₂O were dissolved in 75 ml of DI water. After that, 15 mmol of urea was added into the mixture and stirred for 15 min. The homogeneous solution was transferred to 150 ml Teflon-line stainless steel autoclave, which was heated at 150 °C for a period of 6 h in an oven. The autoclave after heating was naturally cooled down to room temperature for which the precipitate was collected and washed with DI water and ethanol several times by centrifugation and dried at 60 °C overnight. Finally, the pink powder of Ni–Co precursor was obtained.

Synthesis of urchin-like NiCo₂O₄ and NiCo₂S₄ nanoneedles

To synthesize NiCo₂O₄, the obtained precursor was calcined at 300 °C in air for 3 h at a ramping rate of 1 °C min⁻¹. For NiCo₂S₄, the precursor was placed in an alumina boat next to another alumina boat with thiourea powder at the upstream side of tube furnace. Subsequently, the sulfurization process was carried out at 300 °C with a heating rate of 1 °C min⁻¹ under a constant argon flow of 50 sccm for 3 h, and then cooled down to ambient temperature (25 °C).

Physicochemical characterizations

The morphologies of the as-prepared samples were characterized by Field-Emission Scanning Electron Microscopy (FESEM, JSM-7001F, JEOL Ltd.) and Transmission Electron Microscopy (TEM, Hitachi operated at 120 kV). The crystallographic structure was measured by X-ray diffraction (XRD, PHILIPS, X'Pert-MPD 40 kV 35 mA, Cu K α 1.54056 Å) with a 2 θ range between 10–80°. X-ray photoelectron spectroscopy (XPS) was used for the surface analysis

using an AXIS Ultra DLD (Kratos Analytical Ltd., Manchester, UK) with Al-K alpha radiation ($h\nu = 14.866$ eV) as an X-ray excitation source. The electronic properties such as optical band gap energy and work function of the as-prepared materials were studied using UV-Visible near IR spectrometer (UV/Vis/NIR, Lambda 1050, PerkinElmer, USA) and Ultraviolet photoelectron spectrometer (UPS, Riken Keiki, JP). The visible light solar simulator (Newport, Model 67005 sun simulator AM 1.5G/100 mW) was used as a light source.

Electrochemical evaluation

The electrochemical performance of the as-synthesized catalysts including NCO and NCS was investigated using a standard three-electrode system in O₂ and Ar-saturated 0.1 M KOH electrolytes and tested with an AUTOLAB potentiostat (PGSTAT302 N) electrochemical station. For the electrode preparation, a mixture of 10 mg catalyst, 950 μ L iso-propanol, and 50 μ L Nafion solution was ultrasonicated for 30 min to prepare the catalyst ink. Then, 100 μ L of the suspension was loaded on an FTO glass with a working area of 1 cm² (Greatcell Solar Ltd., Australia) and used as a working electrode. A graphite rod and a saturated calomel electrode (SCE) were used as a counter electrode and a reference electrode, respectively. The potentials were calibrated to the reversible hydrogen electrode (RHE) potential using the following equation: E(RHE) = E(SCE) + 0.059pH + 0.241 V. Note that before the measurement, all solutions were purged with Ar gas for 30 min to eliminate impurities. The charge transfer resistance (R_{ct}) was measured using electrochemical impedance spectroscopy (EIS) at 1.55 V vs. RHE under dark and light illumination. The frequency is in a range from 100 kHz to 0.01 Hz. ZABs were assembled using a zinc plate with 50 μ m thickness as the anode and NiCo₂S₄/FTO as the air cathode. The catalyst ink was prepared by mixing active material, carbon black, and PVDF in a ratio of 8 (16 mg): 1 (2 mg): 1 (2 mg) in NMP solution (1 ml). The ink was continuously stirred for 2 h. Then 0.25 ml of the as-prepared ink (4 mg of the active material) was dropped on an FTO glass with an area of 2 × 2 cm². The solvent was allowed to evaporate at 50 °C. The two electrodes were placed in O₂-saturated electrolyte (6 M KOH + 0.2 M Zn(CH₃CO₂)₂ · 2H₂O).

Computational details

All calculations reported in this work were performed by Vienna *ab initio* simulation package (VASP)^[14] based on the periodic plane-wave density functional theory (DFT). The interaction between ion cores and valence electrons was accounted by the projector-augmented wave (PAW)^[15] pseudopotentials. The exchange and correlation interactions between electrons were treated within the generalized gradient approximation (GGA)^[16] with the Perdew-Burke-Ernzerhof (PBE)^[17] parameterization. The additional van der Waals (vdW) contributions were obtained through the semiempirical D2 method of Grimme (DFT-D2).^[18] The effect of 3d electron correlation can be improved by considering on-site Coulomb (U) and exchange (J) interactions. On-site Hubbard term U-J values^[19] of 5.7 and 6.0 eV^[20] were applied for Ni, and Co atoms, respectively. The cut-off energy for the expanded plane-wave basis set was set to 450 eV. The convergence thresholds for full geometry optimizations were set to 10⁻⁵ eV and 0.005 eV/Å for each electronic steps and ionic steps, respectively. Additional details are shown in Section 1 of Supporting Information.

2. Results and Discussion

The morphological and structural analyses were performed using FESEM, TEM, and XRD. The hydrothermally obtained $\text{NiCo}_2(\text{CO}_3)_{0.5}\text{OH}_{0.5}$ precursor exhibits a uniform urchin-like morphology with nanocrystalline self-assembled nanoneedles stemmed radially from the center as shown in Figure S1 (Supporting Information). The formation of hollow nanoneedles can be ascribed to the well-known Kirkendall effect of the sacrificial precursor template during the anion ion exchange process.^[21] The low-magnification FESEM image (Figure 1a) shows that the obtained NiCo_2O_4 was successfully synthesized. After calcination process, the urchin-like morphology remained indicating that this structure is thermally stable. Figure 1b shows the obtained NiCo_2S_4 converted from NiCo_2O_4 after the sulfurization process indicating their excellent structural stability with the remaining morphology. Moreover, high-magnification FESEM images (inset images in Figure 1a–b) also show the morphology of individual microspheres in both NiCo_2O_4 and NiCo_2S_4 forming numerous nanoneedles radially protruded from the center. Interestingly, abundant mesopores can also be observed among the nanoneedles providing more effective surface-active sites and ensuring good accessibility of the electrolyte during the reaction. To give insight into the morphology and structure of the as-prepared NiCo_2S_4 microspheres, the TEM image is shown in Figure 1c. It confirms that each building block of the nanoneedles consists of several interconnected small nanocrystals possessing the porous structure due to the releasing H_2O and CO_2 during the annealing process.^[22] The porous structure of the urchin-like NiCo_2S_4 microspheres was further confirmed by nitrogen adsorption-desorption measurement. As shown in Figure S2a–b (Supporting Information), the adsorption-desorption isotherms of NiCo_2S_4 and NiCo_2O_4 show a type-IV and a type-II isotherms, respectively with a remarkable hysteresis loop at relatively high

pressure indicating their mesoporous characteristics.^[23] The specific surface area of the NiCo_2S_4 is about $83 \text{ m}^2 \text{ g}^{-1}$, which is larger than that of the NiCo_2O_4 (ca. $37 \text{ m}^2 \text{ g}^{-1}$). In addition, the BJH pore size distribution of NiCo_2S_4 microspheres is centered at 4.89 nm, whereas that of NiCo_2O_4 microspheres is around 3.49 nm. High Brunauer-Emmett-Teller (BET) specific surface area and specific pore size distribution can provide tri-phase regions required for the electrochemical reaction and provide effective electron and ion transportation which is beneficial for the electrocatalytic performance. Furthermore, the inset high-resolution TEM image indicates a lattice spacing of 0.28 and 0.33 nm corresponding to the (311) and (220) planes of the NiCo_2S_4 crystal, respectively.^[24] Figure 1d represents the energy-dispersive X-ray mapping (EDX) of the NiCo_2S_4 microspheres with the uniform distribution of Ni, Co, and S elements. In addition, the wavelength dispersive X-ray fluorescence (WDXRF) technique indicates that Ni, Co, and S are the main components with an approximate ratio of 1:2:4, respectively as shown in Table 1.

The crystallographic structure of NCO and NCS was also investigated by XRD as shown in Figure 2a. After the first step of hydrothermal process, the XRD pattern confirms that the nickel-cobalt carbonate hydroxide was successfully grown by matching with $\text{NiCo}_2(\text{CO}_3)_{0.5}\text{OH}_{0.5}$ according to JCPDS no. 48-

Table 1. XRF results of the as-synthesized NiCo_2S_4 .

Element	Composition [%]
S	56.31
Co	28.19
Ni	14.28
Cu	569 ppm
Si	234 ppm
Fe	211 ppm
others	206 ppm

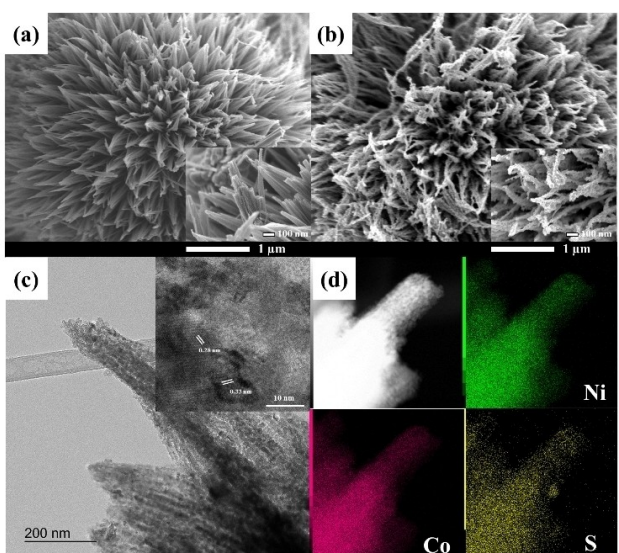


Figure 1. FESEM images at low and high magnification of NCO (a) and NCS (b) and TEM images of NCS (c), and EDX mapping of NCS (d).

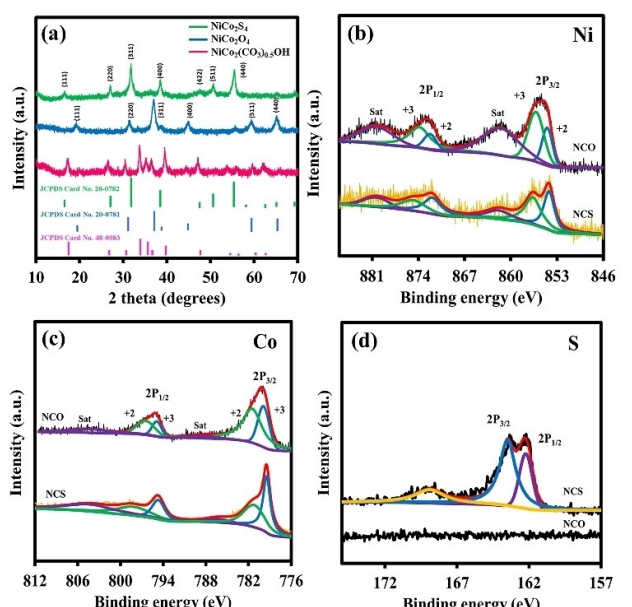


Figure 2. XRD pattern of the as-prepared materials (a), XPS narrow scan spectra of Ni 2p (b), Co 2p (c), and S 2p (d) for NiCo_2O_4 and NiCo_2S_4 .

0083. After the calcination in the second step, the nickel-cobalt carbonate hydroxide hydrate phase was completely transformed into spinel which can be fully indexed to NiCo_2O_4 (JCPDS no. 20–0781). For the urchin-like structure of NiCo_2S_4 composing of several microspheres, the diffraction peaks at 16.5° , 26.9° , 31.7° , 38.4° , 50.5° , and 55.5° can be assigned to 111, 220, 311, 400, 511, and 440 planes of the cubic spinel structure of NiCo_2S_4 (JCPDS no. 20–0782), respectively. It confirms that after the sulfurization process, the NiCo_2S_4 was formed by replacing O^{2-} anions with S^{2-} . As Ni and Co valences can significantly affect the catalytic activity of the electrode, the surface composition and the electronic state of NCO and NCS materials were investigated by XPS as shown in Figure 2b–c. The $\text{Ni } 2p_{3/2}$ spectrum of NCS can be deconvoluted into Ni^{2+} (854.7 eV) and Ni^{3+} (856.2 eV).^[25] The intensity of $\text{Ni}^{2+} 2p_{3/2}$ peak is stronger than that of the $\text{Ni}^{3+} 2p_{3/2}$, suggesting that most of the nickel at the NCS surface consists of Ni^{2+} occupied in the tetrahedral site. In case of $\text{Co } 2p_{3/2}$ spectrum, the binding energies of $\text{Co } 2p_{3/2}$ at 779.8 and 781.1 eV confirm the presence of both Co^{3+} and Co^{2+} in the NCS surface for which Co^{3+} signal is stronger than Co^{2+} due to its higher content. In addition, the two core levels of $\text{Co } 2p_{3/2}$ and $\text{Co } 2p_{1/2}$ obviously show a negative shift about 0.4 and 0.5 eV, respectively compared with the NCO sample. This further indicates the successful formation of NiCo_2S_4 , which is a similar phenomenon to $\text{Ni } 2p_{3/2}$ and $2p_{1/2}$.^[26] These shifts can be mainly attributed to the influence of partial electron transfer between metal sulfide and oxide proving that the introduction of S would remarkably affect the electronic properties of Ni and Co. From the $\text{S } 2p$ spectra of NCS in Figure 2d, the peaks of $\text{S } 2p_{3/2}$ and $2p_{1/2}$ centered at 161.9 and 163.2 eV can be attributed to metal-sulfide (M–S) bond in the NiCo_2S_4 . Moreover, the peak at around 169.1 eV corresponds to the S atom at low coordination near the surface.^[27] These results show that the chemical composition of NiCo_2S_4 contains Co^{2+} , Co^{3+} , Ni^{2+} , Ni^{3+} , and S^{2-} which are in good agreement with the results in previous literature for NiCo_2S_4 .^[28]

The optical and electronic properties of the as-prepared materials were investigated through UV-vis absorption spectrum as shown in the inset of Figure 3a. The NCS displays excellent absorption in the range of 300 to 800 nm which can highly absorb the visible light.^[29] In addition, the absorption band gap energy (E_g) of NCO and NCS can be estimated by the Tauc equation [Eq. (1)]:^[30]

$$(\alpha h\nu)^n = K(h\nu - E_g) \quad (1)$$

Where $h\nu$ is the photoenergy, α is the absorption coefficient, K is a constant relative to the material, and n is either 2 for direct transition or 0.5 for indirect transition. The band gap energies of NCS are calculated to be 1.4 and 2.4 eV while the band gap energies of NCO are 2.0 and 3.3 eV which are consistent with computational calculation (Figure S3a–b, Supporting Information) and those of previous works.^[27] Besides, the valence band (VB) position of NCO and NCS was determined from a Mott-Schottky equation [Eq. (2)]:^[31]

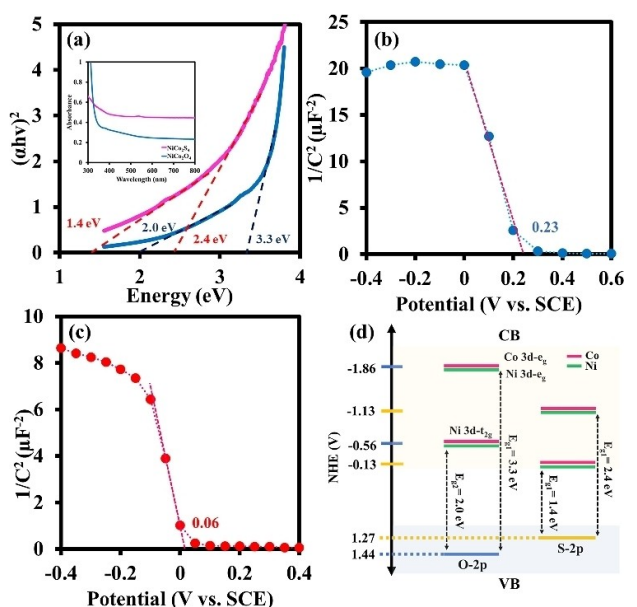


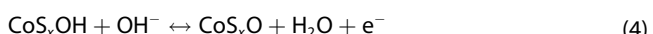
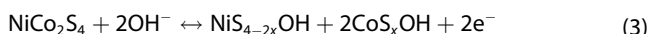
Figure 3. Tauc plots of $(\alpha h\nu)^2$ vs. energy (a) with UV-vis absorption spectra (inset), Mott-Schottky plots of NCO (b) and NCS (c), and the energy diagram of NCO and NCS (d).

$$\frac{1}{C_{cs}^2} = \frac{2}{N_D \epsilon \epsilon_0 e A^2} \left(E - E_{fb} - \frac{kT}{e} \right) \quad (2)$$

where C_{cs} is the interfacial capacitance, ϵ refers to the relative permittivity (dielectric constant), ϵ_0 is the vacuum permittivity, e is the charge of the electron, N_A is the acceptor concentration, E is the applied potential, and E_{fb} is calculated from the intercept extrapolating a straight line from the equation. The C^{-2} vs. E follows a straight line with a negative slope indicating that both NCO and NCS act as p-type semiconductors as shown in Figure 3b–c. The observed flat band potential of NCS is ca. 0.23 V, while NCO is ca. 0.06 V. Note, the energy difference between the top of the VB and E_{fb} is assumed to be 0.2 eV.^[32] Thus, the valence band of NCO and NCS can be estimated at 1.44 and 1.27 V versus normal hydrogen electrode (NHE) which exhibits a similar trend with the UPS result (Figure S4a–b, Supporting Information). As a result, the energy level of NCO and NCS samples can be summarized as shown in Figure 3d. Typically, the electron configuration of the NiCo_2O_4 and NiCo_2S_4 with the cubic spinel structure consists of three spins including one high spin of tetrahedral Co^{2+} ($e_g^4 t_{2g}^3$) and two low spins of octahedral Co^{3+} (t_{2g}^6) and Ni^{3+} ($e_g^1 t_{2g}^6$).^[33] The electron configuration refers to the bands of the NiCo_2S_4 where S 2p orbital is the valence band (VB) and the Co 3d and Ni 3d are the conduction bands (CB). According to this result, the gap energies of NCS are ca. 1.4 eV and ca. 2.4 eV corresponding to the band transition between S 2p and Co 3d-t_{2g} or (Ni 3d-t_{2g}) and from S-2p to Co 3d-e_g (or Ni 3d-e_g), respectively. The gap energies here are lower than those of the NCO catalyst (2.0 and 3.3 eV). It confirms that the NCS catalyst can be easily excited by visible light with expected higher conductive property than the NCO. When the electron is transferred under the photo-excitation, it leaves the positive charge holes which is beneficial

for hydroxide ion in OER reaction. To confirm the photocatalyst properties of NCO and NCS toward OER, the incident-photon-to-current-efficiency (IPCE) technique was applied using a full solar simulator (AM 1.5G/100 mW cm⁻²) equipped with a motorized monochromator (Oriel Cornerstone 130 1/8 m).^[34] The visible light provides the photocurrents of NCO and NCS with the IPCE value of *ca.* 58% and *ca.* 81%, respectively at an applied potential of 1.5 V vs. RHE (Figure S5, Supporting Information). Thus, the energy transition within the band of NCS could be the key factor of superior electrochemical performance as compared to that of the NCO catalyst.

The photo-electrocatalytic activity of the as-prepared NCS material in 0.1 M KOH was investigated by cyclic voltammetry (CV) and linear sweep voltammetry under dark and light illumination. Under dark condition, the CV curve of NCS electrode in Figure 4a shows the redox peaks which can be assigned to Ni²⁺/Ni³⁺ and Co²⁺/Co³⁺/Co⁴⁺ redox couples involving M–S/M–S–OH and M–S–OH/M–S–O reactions.^[35] The possible redox reactions for NiCo₂S₄ are represented as follows [Eq. (3)–(4)]:



In addition, the observed oxidation peak over 1.4 V vs. RHE can be assigned to the OER. The OER overpotential (Figure 4b) at 10 mA cm⁻² of NCS (338.2 mV) is smaller than that of the NCO (384.3 mV) for which the Tafel slope of NCS and NCO are 89.98 and 79.35 mV dec⁻¹, respectively. Whilst, the ORR catalytic activity (Figure 4c) of NCS shows the overpotential at a positive half-wave potential ($E_{1/2}$) of 475.6 mV which is smaller than that of NCO (526.5 mV). This suggests that the NCS exhibits better

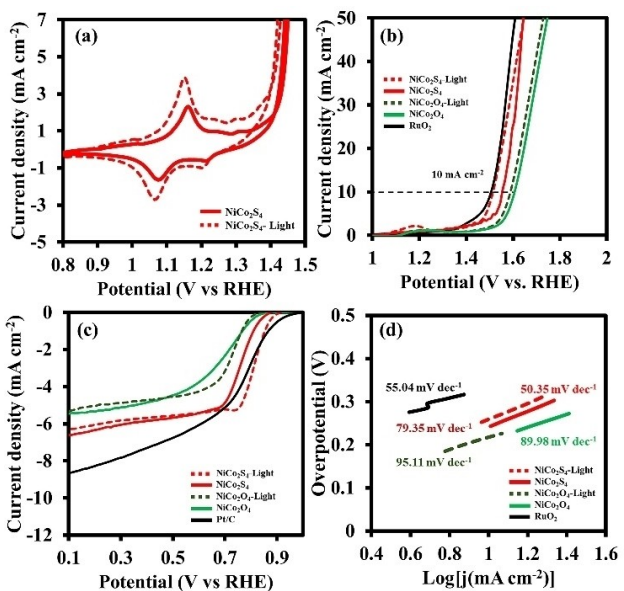


Figure 4. Cyclic voltammetry curve (a), LSVs of OER (b) and ORR (c) with a scan rate of 5 mV s⁻¹, and Tafel plots for NCO and NCS with and without light illumination.

OER/ORR bifunctional catalyst activity and reaction kinetics than the NCO electrode. Interestingly, under light illumination, the larger current density in CV curve with the appearance of redox peaks can be clearly observed as compared to that under dark condition. Note that the performance is based on the photoexcitation related to the optical property of the material. Regarding to the OER activity, the NCS electrode under light illumination shows an overpotential of 285.4 mV which is lower than that of dark condition approaching the value of RuO₂ catalyst (284.7 mV). The photo-enhanced OER performance of NCO and NCS can be approximately estimated to increase *ca.* 2.8% and *ca.* 15.6%. Whilst, the Tafel plot reveals that the NCS under light illumination exhibits a Tafel slope of 50.3 mV dec⁻¹ which is smaller than that under the dark condition. The decrease in Tafel slope indicates that the light illumination to NCS exhibits faster kinetics for the OER process because the narrow energy gap is the key factor rule of the O²⁻/OH⁻ exchange in the OER process which provides easier pathway for the electron transfer in the photoexcitation process. Note, the process with the Tafel value in the range of 60–120 mV dec⁻¹ usually involves two to four electron transfers, whereas the Tafel value below 60 mV dec⁻¹ indicates a four-electron transfer system.^[36] In the opposite direction for ORR, the overpotential of NCS (424.1 mV) under light illumination shows an improved performance about *ca.* 10.8% in comparison with that of NCO (515.3 mV) and about *ca.* 2.2% different from the state-of-the-art Pt/C (428.4 mV) which is more favorably active than other NiCo₂S₄ electrodes (see Table S3, Supporting Information). The durability of NCS was confirmed by the chronoamperometric result as shown in Figure S6, Supporting Information. The normalized current shows a less decay for NCS catalyst after 12 h with a continuous O₂ flow as compared to Pt/C, especially under light illumination. In addition, the cycling stability of OER activity also exhibits good reversibility with negligible decrease in overpotential over 300 cycles as shown in Figure S11 (Supporting Information). Additionally, the charge transfer resistance of photoactive-NCS was studied by the EIS to describe the better catalytic activity compared to that of the NCO as shown in Figure S7 (Supporting Information). The NCS shows a lower charge transfer resistance (R_{ct} of 31.1 Ω) than that under the dark condition (R_{ct} of 43.4 Ω), suggesting that the faster electron transfer is achieved under light illumination. The photoenergy not only reduces the space charge region at the solid-liquid interface which can reduce the overpotential of OER and ORR but also accelerates charge transfer in the system. Furthermore, the density functional theory (DFT) calculations were used to confirm the experimental result. The catalytic activity of OER and ORR of NiCo₂O₄ and NiCo₂S₄ compounds were investigated by the density functional theory (DFT). Figure S8 shows the Gibbs free energy change along the ORR and OER reaction pathways, the calculated Gibbs free energy change relative to H₂O and H₂ indicates that the step of *OH adsorption provides the largest free energy change during the reaction process. The overpotential (η) is the important parameter for comparing the catalytic activities of different catalysts.^[37] The calculated values are shown in Table S1. As a result, the overpotential of NiCo₂S₄

is less than NiCo_2O_4 for both ORR and OER reactions. From this point, it can demonstrate that the NiCo_2S_4 can provide better catalytic activity than the NiCo_2O_4 . Moreover, the computed electronic band structure of NiCo_2O_4 shows higher band gap energy at the high symmetry point gamma (Γ) than the NiCo_2S_4 (Figure S3). This is in good agreement with the experimental study. This smaller energy level gap (Δ) not only improves the conductivity in the intermediate spin-state transformation but also correlates with the ability of photoexcitation resulting in high catalytic performance of NCS over NCO. By the way, the substitution of sulfur atom into the bimetallic also changes the electronic configuration of the material for which the lower energy level of the NCS catalyst provides easier pathway for the electron transfer in the photoexcitation process.

Based on the superior ORR/OER photocatalytic activity of NCS catalyst, a photo-active rechargeable ZAB was fabricated using NCS as the photocatalyst of air-cathode to further demonstrate its practical application under light illumination as shown in Figure 5a. An open-circuit voltage (OCV) of ZAB is *ca.* 1.35 V, which is close to the theoretical value of the equivalent potential between Zn and O_2 (1.65 V vs. Zn).^[38] After the fully discharge process at a current density of 2 mA cm^{-2} , the specific

capacity of NCS under the visible light increased from $646 \text{ mAh g}_{\text{Zn}}^{-1}$ to $734 \text{ mAh g}_{\text{Zn}}^{-1}$, which shifted closer to the theoretical value of the ZAB ($820 \text{ mAh g}_{\text{Zn}}^{-1}$).^[39] During the charging process at 2 mA cm^{-2} with 20 min per cycle, the oxidation reaction of MS with OH^- to M–S–OH and M–S–O follows the reactions (3) and (4).^[40] The discharging process is its reversible process reducing oxygen atoms from the M–S–O structure together with H_2O to produce MS and OH^- namely the ORR process^[41] which is in good agreement with the CV result. Furthermore, the voltage gap of the ZAB under light illumination is *ca.* 0.60 V, which is lower than that under dark condition (*ca.* 0.82 V). This is because the gap energy of NCS electrode can be easily excited by absorbing visible light, generating the photoelectrons in the conduction band and the holes or carriers in the valence band. The highly active photogenerated carriers can easily react with OH^- at the solid-liquid interface, enhancing the photocatalytic evolution of O_2 . The performance of photoactive-ZABs was investigated by discharge-charge tests at a current density of 2 mA cm^{-2} with 10 min a cycle as shown in Figure 5d. ZABs based on the NCS photocatalyst exhibits a stable cycling performance with the charge and discharge potential plateaus at $\sim 1.92 \text{ V}$ and $\sim 1.32 \text{ V}$, respectively. This corresponds to a high energy efficiency of $\sim 68.8\%$ compared to the NCS and precious metal catalyst-based Zn-air battery of $\sim 59.2\%$ and $\sim 63.2\%$ in dark condition. After 60 cycles (600 min), the voltage gap of NCS remains almost constant with a very small increase of 30 mV and finally the cycling stability can be maintained over 230 cycles (2300 h) as shown in Figure S12 (Supporting Information). In contrast to the noble bifunctional catalyst performance, Pt/C and RuO₂ catalysts show an initial voltage gap of 0.63 V which is rapidly increasing to 1.92 V after 30 cycles due to the particle agglomeration and degradation of precious metal catalyst.^[42] As compared to the precious metals of Pt/C and RuO₂, the photoactive NCS with unique urchin-like microstructure not only provides photocatalytic activity in photoactive ZABs but also shows excellent cycling stability. Furthermore, the NCS air electrode could be rapidly charged and discharged at high current densities of 10 and 20 mA cm^{-2} with an outstanding stability over 40 cycles, demonstrating its practical application, as shown in Figure S13, Supporting Information.

3. Conclusions

In summary, a 3D urchin-like NiCo_2S_4 was successfully synthesized using calcination and sulfurization of Ni and Co-based precursors. With the unique intrinsic properties and energy diagrams, the NCS employed as a photocatalyst can simultaneously enhance the visible light absorption in OER and ORR electrocatalysis over the NCO. In addition, the concept of synergistic solar energy capturing into the charge and discharge processes of rechargeable ZABs is introduced for which the semiconducting NCS photoelectrode was used as the air electrode. The NCS-based zinc air battery under light illumination exhibits a lower voltage gap of 0.60 V compared to

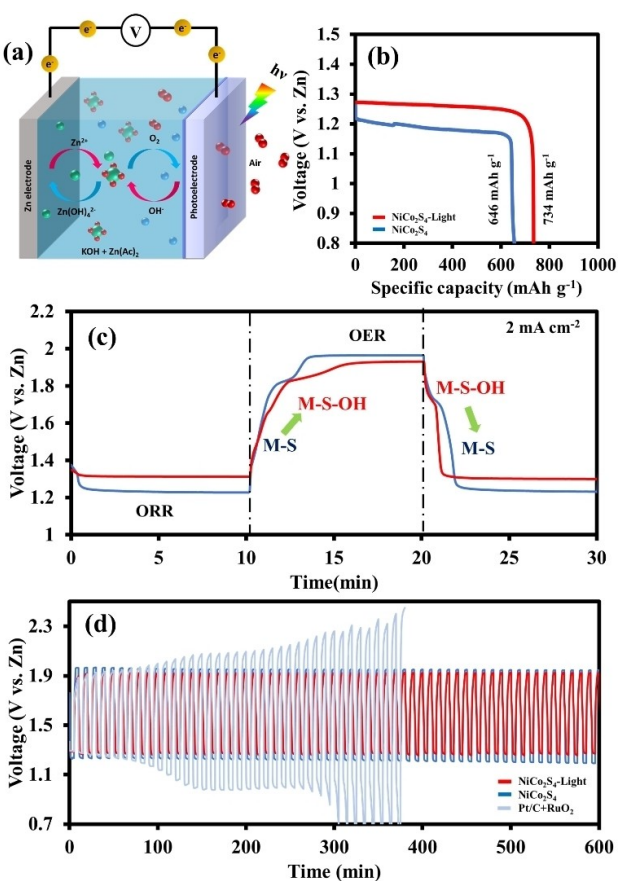


Figure 5. The schematic diagram of photoactive Zn-air batteries with charge and discharge process (a), the discharge curve profile (b), voltage profile of the initial discharge-charge-discharge of the cycling test at 2 mA cm^{-2} with 20 min cycle (c), and the overall discharge-charge profiles of the Zn-air batteries with NCS cathode in the dark and under illumination at 2 mA cm^{-2} (d).

that under dark condition (0.82 V) during charging and discharging due to the generated photoelectrons in the conduction band and simultaneously photo-generated holes in the valence band. The highly active holes can further react with OH⁻ at the solid-liquid interface, enhancing the photocatalytic evolution of O₂. Thus, the strategy being developed in this work reveals that the introduction of semiconductor NCS photoelectrode with an optimized CB and VB positions is promising for an ideal energy conversion and storage with the visible light-driven photocatalytic system to construct zinc-air batteries with high stability and energy efficiency.

Acknowledgements

This work was financially support by Thailand Research Fund and Vidyasirimedhi Institute of Science and Technology (RSA6180031) as well as the Energy Policy and Planning Office (EPPO), Ministry of Energy, Thailand.

Conflict of Interest

The authors declare no conflict of interest.

Keywords: zinc-air batteries • nickel cobalt sulfide • photocatalysts • oxygen evolution reaction • oxygen reduction reaction

- [1] I. Katsounaros, S. Cherevko, A. R. Zeradjanin, K. J. J. Mayrhofer, *Angew. Chem. Int. Ed.* **2014**, *53*, 102–121.
- [2] a) J. Zhang, M. Zhang, Y. Zeng, J. Chen, L. Qiu, H. Zhou, C. Sun, Y. Yu, C. Zhu, Z. Zhu, *Small* **2019**, *15*, 1900307; b) J. Zhang, M. Zhang, L. Qiu, Y. Zeng, J. Chen, C. Zhu, Y. Yu, Z. Zhu, *J. Mater. Chem. A* **2019**, *7*, 19045–19059.
- [3] a) S. Kalasina, P. Pattanasattayavong, M. Suksomboon, N. Phattharasupakun, J. Wuttiprom, M. Sawangphruk, *Chem. Commun.* **2017**, *53*, 709–712; b) S. Kalasina, N. Phattharasupakun, M. Sawangphruk, *J. Mater. Chem. A* **2018**, *6*, 36–40; c) S. Kalasina, K. Kongswatvoragul, N. Phattharasupakun, M. Sawangphruk, *J. Electrochem. Soc.* **2019**, *166*, A2444–A2452.
- [4] a) Y. Liu, N. Li, S. Wu, K. Liao, K. Zhu, J. Yi, H. Zhou, *Energy Environ. Sci.* **2015**, *8*, 2664–2667; b) M. Yu, X. Ren, L. Ma, Y. Wu, *Nat. Commun.* **2014**, *5*, 5111.
- [5] Y. Guo, P. Yuan, J. Zhang, Y. Hu, I. S. Amiinu, X. Wang, J. Zhou, H. Xia, Z. Song, Q. Xu, S. Mu, *ACS Nano* **2018**, *12*, 1894–1901.
- [6] Y. Li, M. Gong, Y. Liang, J. Feng, J.-E. Kim, H. Wang, G. Hong, B. Zhang, H. Dai, *Nat. Commun.* **2013**, *4*, 1805.
- [7] J. Masa, W. Xia, I. Sinev, A. Zhao, Z. Sun, S. Grützke, P. Weide, M. Muhler, W. Schuhmann, *Angew. Chem. Int. Ed.* **2014**, *53*, 8508–8512.
- [8] I. S. Amiinu, Z. Pu, X. Liu, K. A. Owusu, H. G. R. Monestel, F. O. Boakye, H. Zhang, S. Mu, *Adv. Funct. Mater.* **2017**, *27*, 1702300.
- [9] I. S. Amiinu, X. Liu, Z. Pu, W. Li, Q. Li, J. Zhang, H. Tang, H. Zhang, S. Mu, *Adv. Funct. Mater.* **2018**, *28*.
- [10] X.-Y. Yu, X.-Z. Yao, T. Luo, Y. Jia, J.-H. Liu, X.-J. Huang, *ACS Appl. Mater. Interfaces* **2014**, *6*, 3689–3695.
- [11] D. Liu, Q. Lu, Y. Luo, X. Sun, A. M. Asiri, *Nanoscale* **2015**, *7*.
- [12] M. Wang, Y. Lai, J. Fang, F. Qin, Z. Zhang, J. L. K. Zhang, *Catal. Sci. Technol.* **2015**.
- [13] H. S. Jadhav, R. S. Kalubarme, J.-W. Roh, K.-N. Jung, K.-H. Shin, C.-N. Park, C.-J. Park, *J. Electrochem. Soc.* **2014**, *161*, A2188–A2196.
- [14] a) G. Kresse, J. Hafner, *Phys. Rev. B* **1993**, *47*, 558–561; b) G. Kresse, J. Furthmüller, *Comput. Mater. Sci.* **1996**, *6*, 15–50; c) G. Kresse, J. Furthmüller, *Phys. Rev. B* **1996**, *54*, 11169–11186.
- [15] G. Kresse, D. Joubert, *Phys. Rev. B* **1999**, *59*, 1758–1775.
- [16] J. P. Perdew, K. Burke, M. Ernzerhof, *Phys. Rev. Lett.* **1996**, *77*, 3865–3868.
- [17] J. P. Perdew, M. Ernzerhof, K. Burke, *J. Chem. Phys.* **1996**, *105*, 9982–9985.
- [18] G. Stefan, *J. Comput. Chem.* **2006**, *27*, 1787–1799.
- [19] V. I. Anisimov, J. Zaanen, O. K. Andersen, *Phys. Rev. B* **1991**, *44*, 943–954.
- [20] T. Mueller, G. Hautier, A. Jain, G. Ceder, *Chem. Mater.* **2011**, *23*, 3854–3862.
- [21] C. Xia, P. Li, A. N. Gandhi, U. Schwingenschlögl, H. N. Alshareef, *Chem. Mater.* **2015**, *27*, 6482–6485.
- [22] a) J. Li, S. Xiong, Y. Liu, Z. Ju, Y. Qian, *ACS Appl. Mater. Interfaces* **2013**, *5*, 981–988; b) J. Guo, Z. Yin, X. Zang, Z. Dai, Y. Zhang, W. Huang, X. Dong, *Nano Res.* **2017**, *10*, 405–414.
- [23] D. Li, Y. Gong, C. Pan, *Sci. Rep.* **2016**, *6*, 29788.
- [24] R. Zou, Z. Zhang, M. F. Yuen, M. Sun, J. Hu, C.-S. Lee, W. Zhang, *NPG Asia Mater.* **2015**, *7*, e195.
- [25] Y. Xue, Z. Zuo, Y. Li, H. Liu, Y. Li, *Small* **2017**, *13*, 1700936.
- [26] M. A. Peck, M. A. Langell, *Chem. Mater.* **2012**, *24*, 4483–4490.
- [27] H. Chen, J. Jiang, L. Zhang, H. Wan, T. Qi, D. Xia, *Nanoscale* **2013**, *5*, 8879–8883.
- [28] J. Pu, F. Cui, S. Chu, T. Wang, E. Sheng, Z. Wang, *ACS Sustainable Chem. Eng.* **2014**, *2*, 809–815.
- [29] X. Yan, Z. Jin, Y. Zhang, H. Liu, X. Ma, *Phys. Chem. Chem. Phys.* **2019**, *21*, 4501–4512.
- [30] B. Cui, H. Lin, Y.-z Liu, J.-b Li, P. Sun, X.-c Zhao, C.-j Liu, *J. Phys. Chem. C* **2009**, *113*, 14083–14087.
- [31] L. K. Preethi, R. P. Antony, T. Mathews, S. C. J. Loo, L. H. Wong, S. Dash, A. K. Tyagi, *Int. J. Hydrogen Energy* **2016**, *41*, 5865–5877.
- [32] Y. Matsumoto, *J. Solid State Chem.* **1996**, *126*, 227–234.
- [33] a) L. Hu, L. Wu, M. Liao, X. Hu, X. Fang, *Adv. Funct. Mater.* **2012**, *22*, 998–1004; b) I. T. Papadas, A. Ioakeimidis, G. S. Armatas, S. A. Choulis, *Adv. Sci.* **2018**, *5*, 1701029–1701029.
- [34] G. Dong, H. Hu, X. Huang, Y. Zhang, Y. Bi, *J. Mater. Chem. A* **2018**, *6*, 21003–21009.
- [35] Y. Liu, Z. Wang, Y. Zhong, M. Tade, W. Zhou, Z. Shao, *Adv. Funct. Mater.* **2017**, *27*.
- [36] N.-T. Suen, S.-F. Hung, Q. Quan, N. Zhang, Y.-J. Xu, H. M. Chen, *Chem. Soc. Rev.* **2017**, *46*, 337–365.
- [37] Y. Jiao, Y. Zheng, M. Jaroniec, S. Z. Qiao, *Chem. Soc. Rev.* **2015**, *44*, 2060–2086.
- [38] Y. Li, H. Dai, *Chem. Soc. Rev.* **2014**, *43*, 5257–5275.
- [39] J.-S. Lee, S. Tai Kim, R. Cao, N.-S. Choi, M. Liu, K. T. Lee, J. Cho, *Adv. Energy Mater.* **2011**, *1*, 2–2.
- [40] B. Li, J. Quan, A. Loh, J. Chai, Y. Chen, C. Tan, X. Ge, T. S. A. Hor, Z. Liu, H. Zhang, Y. Zong, *Nano Lett.* **2017**, *17*, 156–163.
- [41] C. Tomon, S. Sarawutanukul, S. Duangdangchote, A. Krittayavathananon, M. Sawangphruk, *Chem. Commun.* **2019**, *55*, 5855–5858.
- [42] D. Bin, Z. Guo, A. G. Tamirat, Y. Ma, Y. Wang, Y. Xia, *Nanoscale* **2017**, *9*, 11148–11157.

Manuscript received: December 9, 2019

Revised manuscript received: January 30, 2020

Accepted manuscript online: February 3, 2020

Version of record online: March 6, 2020